Journal of Energy Chemistry 26 (2017) 1282–1290

Contents lists available at ScienceDirect

Journal of Energy Chemistry

journal homepage: www.elsevier.com/locate/jechem

http://www.journals.elsevier.com/journal-of-energy-chemistry/

Nitrogen-doped hierarchical porous carbon derived from metal–organic aerogel for high performance lithium–sulfur batteries

Han Zhang[a], Zongbin Zhao[a,*], Yang Liu[a], Jingjing Liang[a], Yanan Hou[a], Zhichao Zhang[b], Xuzhen Wang[a,b], Jieshan Qiu[a,*]

[a] State Key Lab of Fine Chemicals, Liaoning Key Lab for Energy Materials and Chemical Engineering, PSU-DUT Joint Center for Energy Research, School of Chemical Engineering, Dalian University of Technology, Dalian 116024, Liaoning, China
[b] School of Chemistry, Dalian University of Technology, Dalian 116024, Liaoning, China

ARTICLE INFO

Article history:
Received 20 July 2017
Revised 28 August 2017
Accepted 29 August 2017
Available online 14 October 2017

Keywords:
Metal–organic aerogel
N-doped porous carbon
Lithium–sulfur batteries

ABSTRACT

Nitrogen-doped three-dimensional (3D) porous carbon materials have numerous applications due to their highly porous structures, abundant structural nitrogen heteroatom decoration and low densities. Herein, nitrogen doped hierarchical 3D porous carbons (NHPC) were prepared via a novel metal–organic aerogel (MOA), using hexamethylenetetramine (HMT), 1,3,5-benzenetricarboxylic acid and copper (II) as starting materials. The morphology, porous structure of the building blocks in the NHPC can be tuned readily using different amount of HMT, which makes elongation of the pristine octahedron of HKUST-1 to give rise to different aspect ratio rod-like structures. The as-prepared NHPC with rod-like carbons exhibit high performance in lithium sulfur battery due to the rational ion transfer pathways, high N-doped doping and hierarchical porous structures. As a result, the initial specific capacity of 1341 mA h/g at rate of 0.5 C (1 C = 1675 mA h/g) and high-rate capability of 354 mA h/g at 5 C was achieved. The decay over 500 cycles is 0.08% per cycle at 1 C, highlighting the long-cycle Li–S batteries.

1. Introduction

In the recent decades, the demands for high-efficiency electrical energy storage technologies are growing in importance with the impendent shortage of fossil energy and environmental problems such as global warming and atmospheric pollution [1]. Lithium-sulfur batteries based on the high voltage electrochemical reaction between sulfur and lithium are one of the most outstanding candidates due to its ultrahigh energy density (2600 Wh/kg) and theoretical capacity (1675 mAh/g). Furthermore, sulfur has the advantages of low cost, high abundance and environmentally friendly. However, some issues need to be solved before its wide applications for Li–S batteries. Firstly, the low electrical conductivity (5×10^{-28} S/m) of sulfur results in limited utilization of active material and poor electrochemical activity. Secondly, lithium polysulfide (LiPS) is easily dissolved in organic electrolytes during the charge/discharge electrochemical process, and cause "shuttle effect" between the electrodes, thus leading to a successive loss of active materials [2]. Thirdly, the dramatic volume expansion (over 70%) of sulfur during the charge/discharge seriously reduces the cycling stability [3,4].

Over the last decades, some considerable methods have been developed to solve these issues. The use of carbon materials as the host scaffold conductive framework to obtain a nanostructured composite sulfur cathode becomes an effective approach to improve electrical conductivity and the utilization of S. Carbon based materials, such as porous carbon [5,6], graphene [7–10], carbon nanofibers [11–14], carbon nanotubes [15–18], as well as conductive polymer [19], have been widely used for the construction of high performance electrodes in Li–S batteries [20,21]. The most of charge/discharge generated LiPS are limited in the conducting porous host framework and can be improved effectively the capacities and static cycle. However, the weak force between polar LiPS and nonpolar carbon leads to LiPS leakage, resulting in a poor cycle stability [22,23]. It has been discovered that some metal oxides (e.g., TiO_2 [24], MnO_2 [25,26], Ti_4O_7 [27,28], SiO_2 [29], ITO [30]), metal sulfides (e.g., TiS_2 [31], WS_2 [32]), metal-carbides (MXene phases [33]), and metal–organic frameworks [34–37] have achieved more success due to their more effective polysulfide binding via chemical interaction or surface-mediated redox reaction. However, the high mass ratio of the metal-based materials can inevitably reduce the mass energy density of the batteries.

* Corresponding authors.
E-mail addresses: zbzhao@dlut.edu.cn (Z. Zhao), jqiu@dlut.edu.cn (J. Qiu).

https://doi.org/10.1016/j.jechem.2017.08.016

Recently, functionalization of ultralight, high specific surface area porous carbons doped with heteroatom have been regarded as one of potentials for LiPS confinement [38,39], for example, N-doped porous carbons show high conductivity and excellent chemisorption of LiPS resulted from the electron donating property of nitrogen [40]. One-dimensional (1D) carbon materials (e.g., carbon nanorods [6], carbon nanofibers [11], carbon nanotubes [16]) could easily form an efficient pathway for electron and lithium ions during the charge/discharge.

Based on these considerations mentioned above, metal–organic frameworks (MOFs) and metal–organic aerogel (MOA) were chosen as the precursor for the preparation of porous carbon materials [41–44]. MOA consists of metal ions and organic ligands and can retain the morphologies and porous structures after carbonization under high temperature [45–48]. Yang et al. [35] reported sulfur/MOF-derived hierarchical porous carbon fibers for lithium–sulfur batteries. The introduction of 1D-orientation carbon network with high electrical conductivity results in improved capacity.

Herein, a novel N-doped hierarchical porous carbons (NHPC) with rod-like nanostructures have been fabricated and used as sulfur host material for the high-performance lithium-sulfur batteries. The hierarchical porous carbon rods designed in this work offer several structural and composition advantages: (i) a high specific surface area and abundant pore structure, effectively improving the physical confinement of LiPS and sulfur loading; (ii) 3D conductive framework and hierarchical porous structures provide a significant pathway for electron and lithium ions transport; (iii) the N atom doping can increase chemisorption ability of LiPS.

2. Experimental

2.1. Synthesis of MOA-x

0.21 g 1,3,5-benzenetricarboxylic acid (BTC, 1 mmol) and 0.14 g hexamethylenetetramine (HMT, 1 mmol) were dissolved into 20 mL of deionized water and stirred at room temperature for 1 h. Then, 0.36 g copper (II) nitrate hydrate (1.5 mmol) was dissolved into 20 mL deionized water and poured into the above solution. The two solutions were rapidly mixed together, shaken for several times. A metal organic hydrogel (MOH) was obtained after 1 h. After freeze-drying for 48 h, the solvent within the MOH was completely removed and the metal organic aerogel (MOA) was produced. The molar of HMT added to the system is adjusted (0.1, 0.5, 1 and 2 mmol) to give carbon materials with different structures, the obtained samples are denoted as MOA-*x*, where *x* represents for the molar ratio of HMT to BTC.

2.2. Synthesis of NHPC and S/NHPC

The Cu containing N-doped porous carbons were prepared by thermal treatment of MOA with a ramp rate of 2 °C/min at a series of temperature ranging from 600 °C to 900 °C for 2 h in the protection of N_2. The as-prepared Cu/N-doped porous carbon composite was denoted as Cu-NPC. The Cu nanoparticles were removed by 1 M $FeCl_3$ aqueous solution for 24 h. The resulting N-doped hierarchical porous carbon (NHPC) were collected by washing several times with deionized water and then dried at 60 °C overnight. The S/NHPC nanocomposite was prepared using a melt-diffusion strategy [2]. Typically, sublimed sulfur was mixed homogeneously with NHPC power with a mass ratio of 3:1 or 1:1. Then, the mixture was heated at 155 °C for 12 h in stainless steel vessels with argon gas flow. S/NHPC possesses with a sulfur content of 74%. Sulfur contents were determined by thermogravimetric analysis (TGA) (Fig. 1).

2.3. Synthesis of HKC and S/HKC

0.21 g 1,3,5-benzenetricarboxylic acid (BTC, 1 mmol) and 0.36 g copper (II) nitrate hydrate (1.5 mmol) were firstly dissolved into a mixture of 20 mL deionized water and 20 mL ethanol under stirring and kept for 24 h. After stirring, the blue powder was collected by centrifugation and washed with deionized water and ethanol for three times. The product was then freeze-dried for further experiment and characterizations, which was named as HKUST-1. The HKC was prepared from HKUST-1 under the same procedure for NHPC. And S/HKC (sulfur 71 wt%) was prepared similarly to S/NHPC (Fig. 1).

2.4. Characterization

The morphology of products was characterized by scanning electron microscopy (SEM, QUANTA 450) and field-emission scanning electron microscopy (FESEM, SUPARR 55). The crystalline phases of the products were examined using Rigaku D/MAX-2400 diffractometer (XRD) equipped with a rotating anode and a Cu$K\alpha$ radiation source ($\lambda = 0.15418$ nm). X-ray photoelectron spectroscopy (XPS) analysis was performed using a Thermo ESCALAB 250 spectrometer employing an Al-$K\alpha$ X-ray source. Thermal stability of the samples were assessed by thermal gravimetric analysis (TGA, DTG-60AH) in nitrogen with temperature ranging from 30 °C to 500 °C at a heating rate of 10 °C/min. Elemental analysis (Vario EL III) was performed to determine the elemental composition of the samples. N_2 adsorption/desorption isotherms were measured with a Micromeritics 3Flex 3500. The composites were degassed at 250 °C for 5 h prior to the nitrogen adsorption measurement.

2.5. Electrochemical measurements

The electrochemical measurements were conducted using CR2026 coin cells with pure Li foil as the counter and reference electrode at room temperature. The working electrode consists of a test material (for example, S/MOC or S/HKC nanocomposite), acetylene black and polyvinylidene difluoride (PVDF) in a weight ratio of 7:2:1. Then working electrodes were fabricated by slurry casting on Al foil. The electrodes were dried at 60 °C overnight. Coin type cells were assembled in a glove box under argon atmosphere (water and oxygen concentration less than 0.1 ppm). For Li–S batteries, it consisted of a prepared electrode, polypropylene separator, and lithium foil as the counter electrode. The electrolyte used in this experiment was 1.0 M Li bis(trifluoromethanesulphonyl)imide (LiTFSI) in 1,3-dioxolane and 1,2-dimethoxyethane (1:1 by volume) with 1.0 wt% $LiNO_3$ additive. The amount of electrolyte in a single cell is 30 μL with sulfur loading concentration (the ratio of molar amount of sulfur in the composite cathode to the volume of electrolyte encapsulated in a single cell) of 1.97 mol/L. The galvanostatic charge/discharge tests were carried out on a Land CT2001A battery test system between 1.5 and 3.0 V using 2016 coin-type cells. The cyclic voltammograms (CV) was conducted using a multichannel electrochemical workstation (VMP-300) between 1.5 and 3.0 V at a scan rate of 0.1 mV/s. Electrochemical impedance spectroscopy was performed using a CHI 660D electrochemistry workstation by applying an AC amplitude of 5 mV over the frequency range from 0.01 to 105 Hz.

3. Results and discussion

Firstly, copper (II) nitrate hydrate, 1,3,5-benzentricarboxylic acid and HMT were mixed in water solution to form wet gels. The as-synthesized gels were dried by freeze-drying, resulting in MOA. We demonstrated that various gels of Co-BTC, Zn-BTC and Cr-BTC can be also successfully prepared with the similar procedure (Fig.

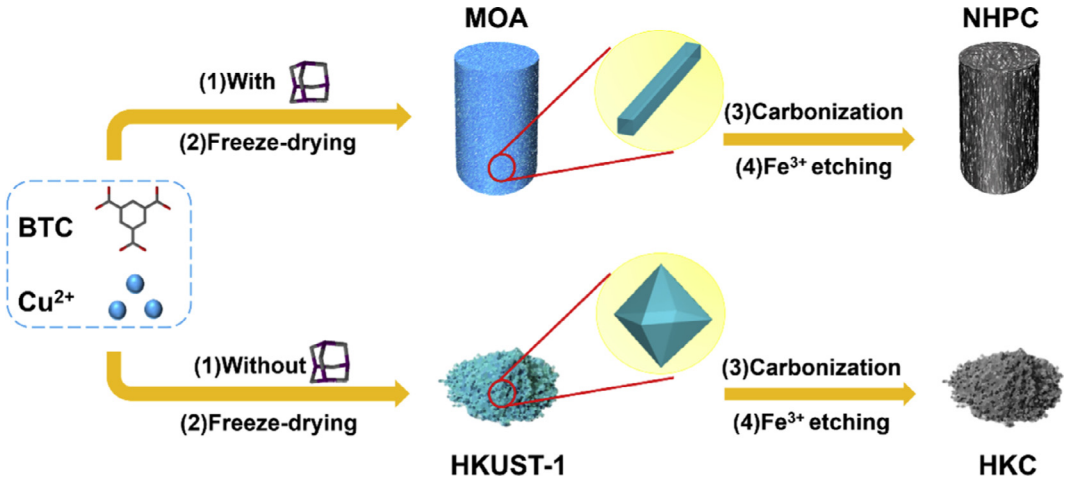

Fig. 1. Schematic diagram of the synthesis process of the NHPC and HKC.

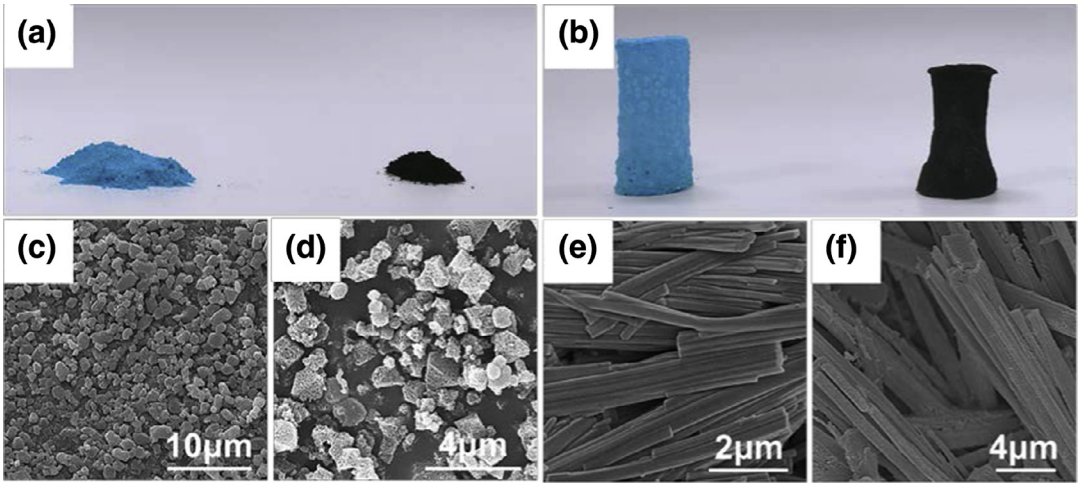

Fig. 2. Digital photographs of (a) HKUST-1 and HKC, (b) MOA and NHPC. Scanning electron microscopy (SEM) images of (c) HKUST-1, (d) HKC, (e) MOA-1, (f) NHPC-1.

S1), suggesting the versatility of this strategy. Then the as-prepared MOA was directly carbonized at high temperature in N_2 gas flow to produce Cu/nitrogen-doped porous carbon composites (Cu-NPC). NHPC was finally obtained after the subsequent removal of Cu in the Cu-NPC with aqueous solution of $FeCl_3$. HKC was prepared with the similar procedure but without the addition of HMT, in this way powder materials were obtained instead of monolith carbon materials. Finally, sulfur is loaded into NHPC and HKC by a melting-diffusion method for the application in lithium sulfur battery.

The digital photograph of HKUST-1 is shown in Fig. 2(a), blue powder can be seen. After the annealing at elevated temperature and etching processes, black powder HKC was finally obtained. SEM image of HKC (Fig. 2(d)) shows that the octahedron of the HKUST-1 is retained with a contracted size. However, the addition of HMT in the reaction system remarkably changes the structure of materials (Figs. 2(b) and S2). It can be observed that blue gels are obtained instead of liquid dispersion. The morphology of the as-synthesized MOA-1 is investigated using SEM (Fig. 2(e)), which reveals rod-like structures with smooth surfaces, a length in the range of 3–10 μm and the diameter of 200–300 nm. After the carbonization of MOA-1, the resultant NHPC-1 (Fig. 2(f)) shows a rod-like shape inherited from MOA-1. The compactly assembled carbon rods in parallel creates interconnection among them, which is expected to offer an effective pathway for fast electron transport. Fig. S4 gives a typical EDS elemental mapping analysis of the S/NHPC-1, evidently revealing the homogenous distribution of C, N, and S along the whole rods. Obviously, nitrogen atom was uniformly doped in the hierarchical porous carbon and no aggregated sulfur particles can be observed even in a magnified image.

The influence of HMT on the formation of products was investigated in detail. Fig. 3 shows the representative SEM images of the as-synthesized products prepared with different amount of HMT (e.g., mole ratio of H_3BTC/HMT). As shown in Fig. 3(a)–(d), the pristine HKUST-1 from blue dispersion was revealed by SEM to be typical octahedrons. However, when a small amount of HMT (1:0.1) was added, light blue gels were obtained instead of blue dispersion. SEM image clearly reveals that the MOA-0.1 possesses a rhombic shape with an edge length of 200–500 nm. This rhombic shape seems to be the elongation of the pristine octahedron of HKUST-1 (Fig. 3(a)). More interestingly, a further increased amount of HMT (1:0.5) gives rise to the growth of short rod-like crystals (Fig. 3(c)). Obviously, as shown in Fig. 3(d), the aspect ratio of rods increases with the increasing of HMT (1:1). However, in the case of adding extra amount of HMT (1:2, Fig. 3(e)), the shape of MOA-2 turns out to be nanoparticles, implying the collapse of rod-like structure. It should be noted that the C content of NHPC-2 decreases remarkably compared with the NHPC-1 (Table S1), this is consistent with the carbon structure transformation from rods to nanoparticles. Furthermore, digital images show that excess HMT inhibits the formation of gel (Figs. 3(e) and S2(f)). The

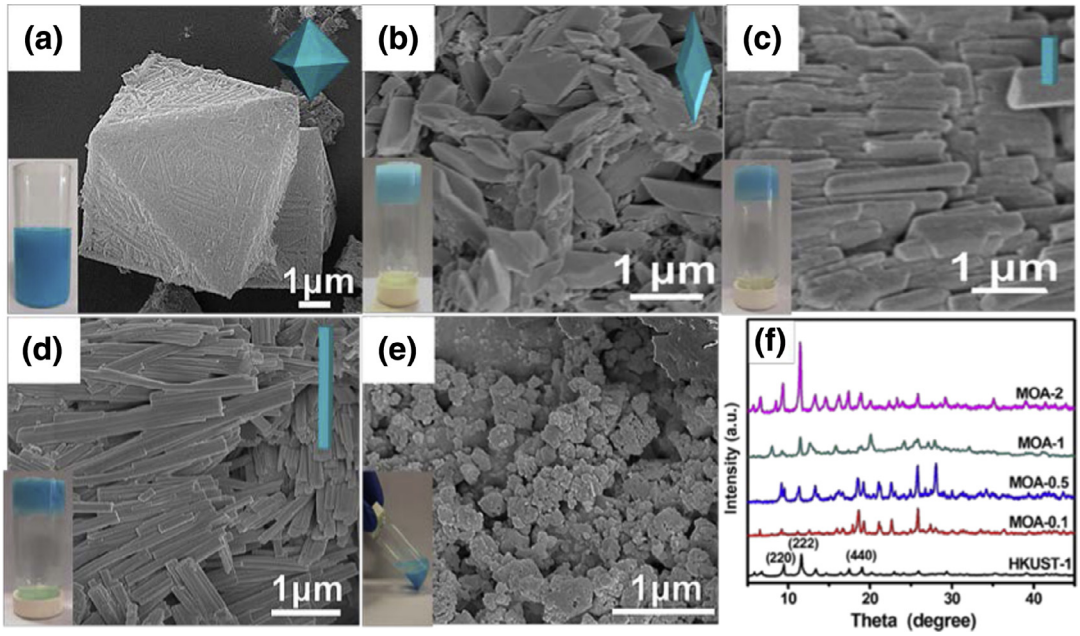

Fig. 3. SEM images of (a) HKUST-1, (b) MOA-0.1, (c) MOA-0.5, (d) MOA-1, (e) MOA-2; (f) XRD patterns of the HKUST-1, MOA-0.1, MOA-0.5, MOA-1 and MOA-2.

morphologies of the corresponding carbon materials are shown in Fig. S5. The MOA was examined by XRD (Fig. 3(f)), which exhibited well-recognized diffraction patterns, showing both the broad characteristic diffraction peak at ~11° and 13° indexed to the (220) and (222) planes of the HKUST-1, respectively, implying that the as-synthesized MOA kept the crystalline and porous structure of HKUST-1.

In comparison with HKUST-1, the addition of HMT created a new feature peaking at 40–140 cm^{-1} in Raman spectra, which could be attributed to the N–Cu–N bonding (Fig. 4(a)) [49]. Meanwhile, the XPS spectra of MOA-1 in the range from 924 to 964 eV are ascribed to Cu 2*p* (Fig. 4(b)). The well-known "shake-up satellite bands" (at 938–946 eV) are clearly shown, which is representative of paramagnetic chemical state of Cu^{2+}. For MOA-1, a slight binding energies change of Cu $2p_{3/2}$ shifted from 934.5 to 935 eV. In comparison with HKUST-1, the intensities of "shake-up satellite bands" peaks also had a slightly reduced. These binding energy shifts should owe to the Cu^{2+} accepting the lone pair electrons from donating by HMT [50]. Meanwhile, the high-resolution N 1*s* spectrum, three peaks at 400.0, 401.6 and 406.9 eV can be corresponding to Cu–N, C–N–H and C_3–N (Fig. 4(c)). The above XPS results demonstrate that there is a convincing association between Cu^{2+} center and N. The mechanism of MOA forming progresses, Cu and N coalesce interactions in a nascent network of gel material were shown in Fig. 4(d) and endorsed by experimental observations.

The samples were further examined with XRD (Fig. 5(a)). The XRD profiles of HKC and NHPC-1 show two broad signals at ~24° and ~44° indexed to the (002) and (100) planes, respectively. These broad peaks indicate that both HKC and NHPC-1 are featured with amorphous structures. The sulfur is loaded into NHPC-1 and HKC by a melting-diffusion method, the S/HKC and S/NHPC-1 are identified and all the prominent peaks can be corresponding to orthorhombic sulfur (JCPDS no: 08-0427) by XRD. Despite both the sulfur loading of composite materials are over 70%, the intensities of the characteristic peak in the S/HKC and S/NHPC-1 samples are still weak, meaning the uniform dispersion of nano-sized sulfur within the carbon host. In Raman spectra of the finger-print peaks of carbon samples, the peak of D band at 1354 cm^{-1} is corresponded to the existence of structural disorder and defects in carbon material, while the G band at 1587 cm^{-1} is assigned to the stretching vibration of any pair of sp^2 sites inside the graphitic pattern. The ratios of the relative intensity of the D band to the G band (I_D/I_G) of NHPC-*x* were found to increase with the increasing of HMT (Fig. 5(b) and Table S1), which implies the addition of the HMT increases the defect sites of the resultant carbon materials.

To further identify the pore texture of the HKC and NHPC-1, nitrogen adsorption-desorption characterization was carried out and the results were shown in Fig. 5(c) and (d) Both the HKC and NHPC-1 exhibit similar isotherm type IV following the IUPAC classification, implying that the pore structure have abundant mesopores. The pore size distributions determined using the QS-DFT model indicate that the materials consist of three peaks located at 0.8, 3 and 15 nm, mostly in the range of micropores and mesopores. The BET surface areas of the HKC and NHPC-1 are 704 and 730 m^2/g, meanwhile, the total pore volumes of the HKC and NHPC-1 are 0.77 cm^3/g and 0.81 cm^3/g (Table S2). It is noteworthy that both NHPC-1 and HKC have hierarchical porosity structures, which can help to hold the LiPS during cycling, the efficient contact between Li ions and sulfur active material and accelerate the fast ion transportation [51,52].

For understanding the chemical valence and elemental composition of S/NHPC-1 and S/HKC, XPS analyses have been performed (Figs. 5(e) and (f) and S6). The survey scan of S/NHPC-1 reveals the presence of C, O, N and S. The XPS of C 1*s* spectrum, has a major peak corresponding to sp^2-hydridized carbon at 284.6 eV, as well as the peak at 285.1 eV is assigned to C–N/C–S, revealing the chemical bonding between elemental sulfur and N-doped porous carbon (Fig. S6(a)). Moreover, two weak peaks at 286.7 eV and 288.8 eV, which can be ascribed to C–O and O–C=O [5]. The three peaks at 398.2, 400.5, and 402.5 eV in the N 1*s* spectrum corresponds to pyridinic N, pyrrolic N, and graphitic N, respectively (Fig. 5(e)) [53]. The first two N types are dominant in the product, which are believed to be more effective in forming S_xLi–N interactions via the N lone-pair electrons [38]. The XPS of S 2*p*, the peaks at 163.4 eV and 164.6 eV are attributed to S $2p_{3/2}$ and $2p_{1/2}$, respectively. The S $2p_{3/2}$ binding energy of S/NHPC-1 is slightly lower than that of pure S [54], implying the conceivable presence of C–S bond. The

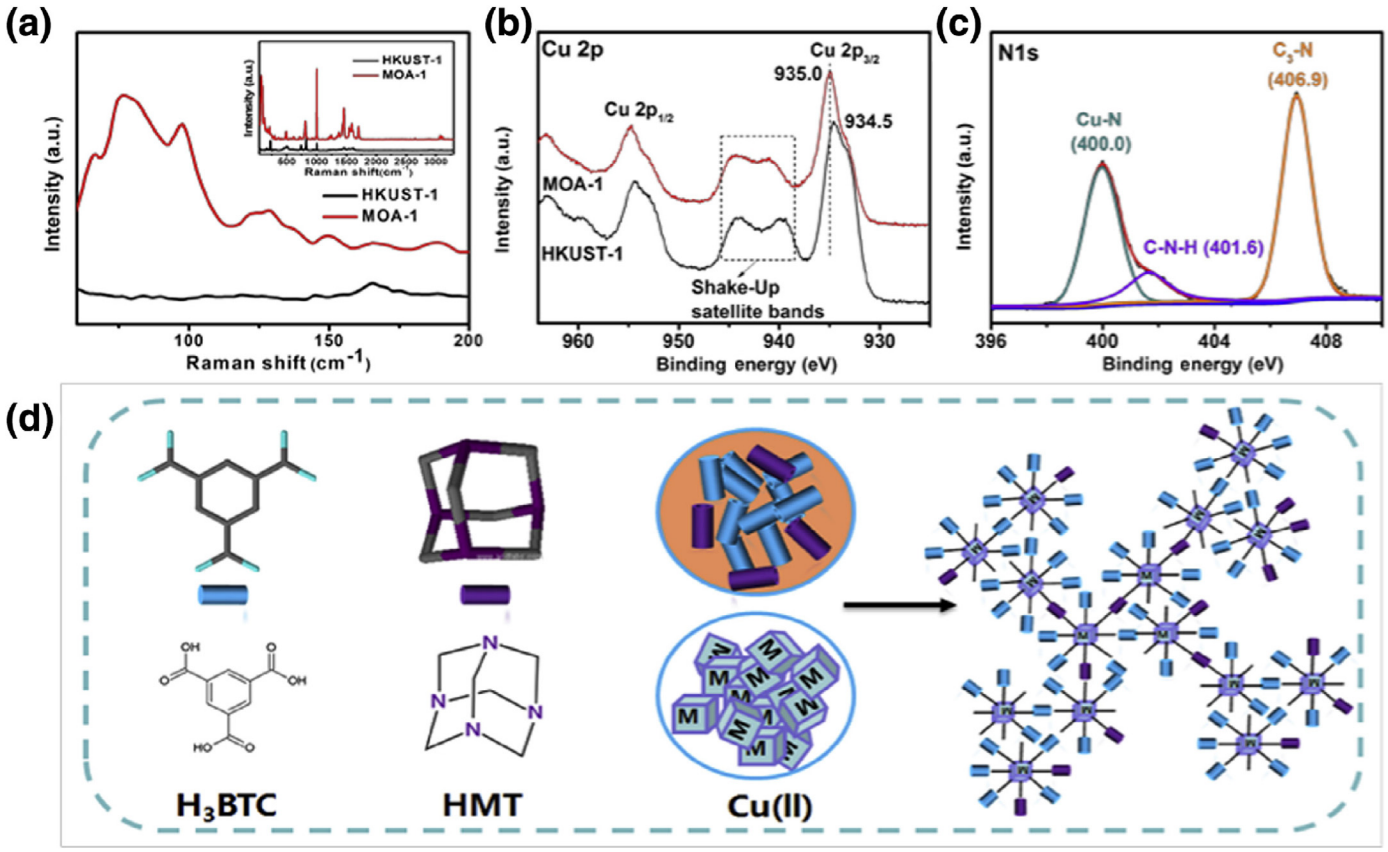

Fig. 4. (a) Raman spectra of HKUST-1 and MOA-1. (b) X-ray photoelectron spectroscopic (XPS) survey spectrum and high-resolution Cu 2*p* of HKUST-1 and MOA-1. (c) XPS spectrum in the N 1*s* of MOA-1. (d) Schematic diagram of the proposed formation mechanism underpinning growth of MOA 3D network.

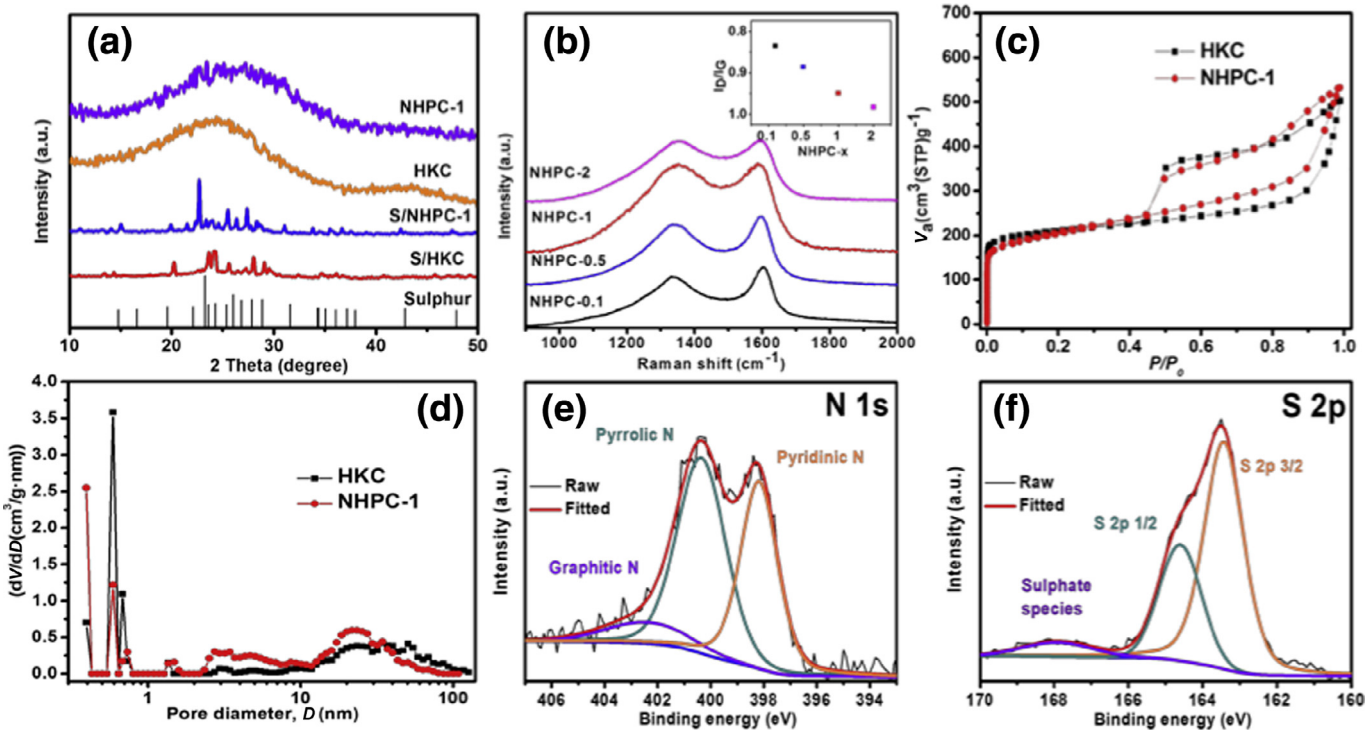

Fig. 5. (a) XRD patterns of the S/HKC, S/NHPC-1, HKC, NHPC-1 and sulfur powder. (b) Raman spectra of NHPC prepared with different amounts of HMT. (c) N_2 sorption isotherms at 77 K. (d) Pore size distributions of the HKC and NHPC-1. XPS survey spectrum of S/NHPC-1: (e) N 1*s* and (f) S 2*p*.

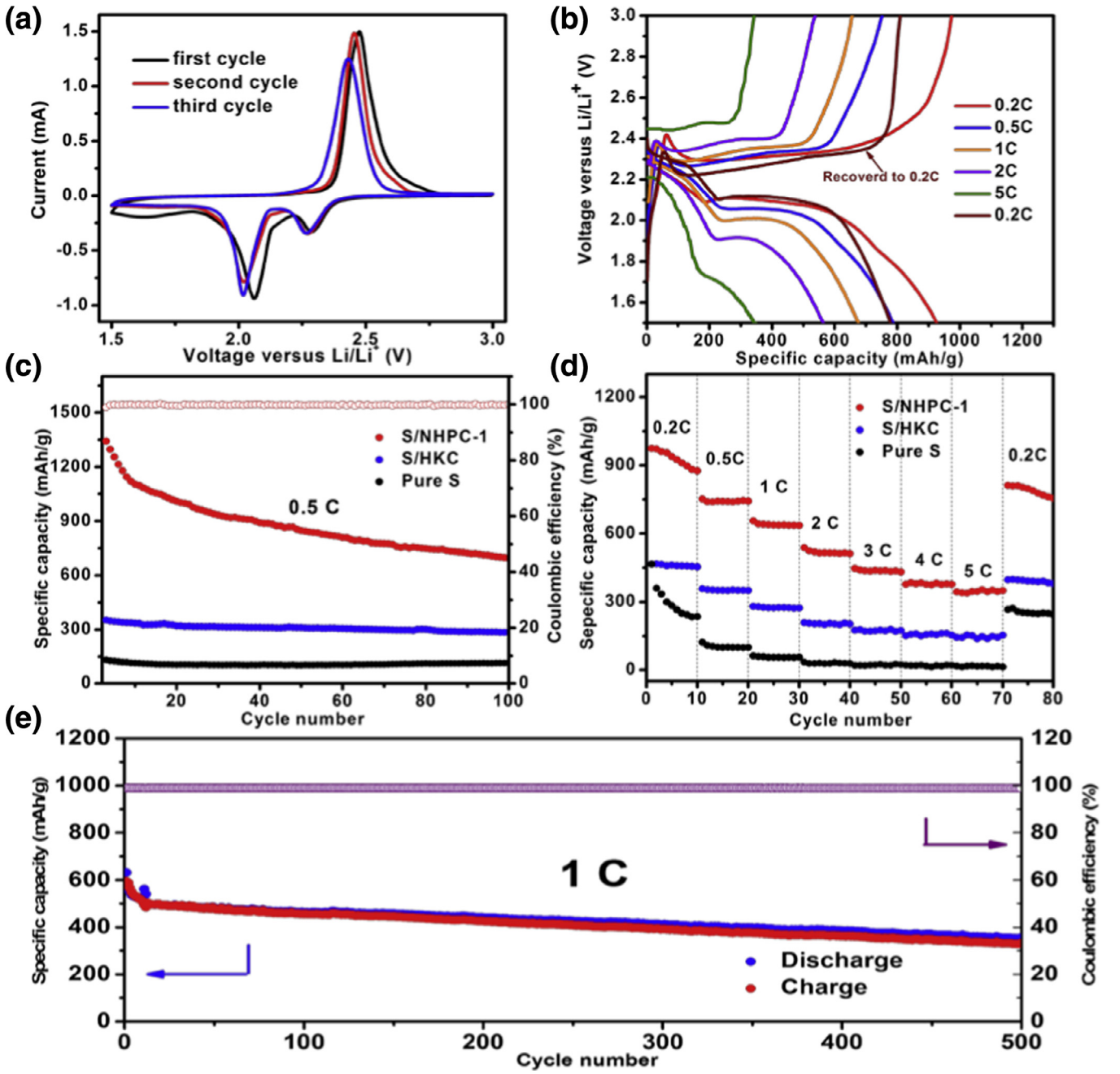

Fig. 6. (a) Cyclic voltammograms (CVs) and (b) galvanostatic charge/discharge curves at current rate of 0.2, 0.5, 1, 2, 3, 4 and 5 C tested between 1.5 and 3.0 V of S/NHPC-1. (c) Performance data of S/NHPC-1, S/HKC and pure S tested at a rate of 0.5 C. (d) Rate performance of S/NHPC-1, S/HKC and pure S at 0.2 C to 5 C. (e) Long-term cyclic of S/NHPC-1 tested at 1 C.

peak at 166.5–170 eV is assigned to the sulfate species formed by sulfur oxidation in air [22]. Consequently, the XPS results clearly demonstrate the successful doping of the carbon framework with N atoms and the surfaces functional group of S/NHPC-1. The N of S/NHPC-1 derived from HMT is beneficial to the immobilization of polysulfide intermediates [9,55,56]. The content of sulfur in S/NHPC-1 and S/HKC were estimated by thermalgravimetric analysis (TGA). As featured by the TGA curve (Fig. S8), the S/NHPC-1 and S/HKC show a weight loss of 74% and 71% at 500 °C, respectively, which can be ascribed to the sublimation of sulfur.

The Li foil as lithium–sulfur anode and synthesized materials as cathode material fabricated the coin cells to assess the battery performance. As shown in Fig. 6(a), the cyclic voltammetry of S/NHPC-1 was measured at a scan rate of 0.1 mV/s between 1.5 and 3.0 V. Two main reduction peaks were detected at 2.26 V and 2.05 V, indicating that the two-step stages of sulfur during the first scan. According to the reported mechanism, the peak at 2.26 V are assigned to the process from sulfur to Li_2S_n ($4 \le n \le 8$), while the peak at about 2.05 V are assigned to the process from Li_2S_n ($4 \le n \le 8$) to lower-order polysulfide ions (Li_2S_2 and Li_2S). Similarly, for the anodic scan, only an oxidation peak at about 2.43 V was attributed to the process from Li_2S to element sulfur. After the first cycle scan, the peak positions and intensities shows negligible change, implying that the S/NHPC-1 possesses good charge/discharge reversibility. The galvanostatic charge-discharge profiles of S/NHPC-1 at different rate of current density are shown in Fig. 6(b) and the evident voltage plateaus existing in the curves are in agreement with the peaks of CVs. Two obvious reaction plateaus and an oxidation

plateau can be clearly observed, indicating that S_8 and Li_2S can transform into each other during charge/discharge [57]. We display the cycling performance of the S/HKC, pure S and rod-like structure of S/NHPC-1 cathodes at current density of 0.5 C in a voltage range of 1.5 –3 V, shown in Fig. 6(c). For the S/HKC cathodes, only a low initial discharge capacity of 352 mAh/g is obtained. Then it quickly drops to 318 mAh/g in the first 20 cycles, finally gradually decreases to 283 mAh/g after 100 cycles and those of pure sulfur (197 mAh/g). The capacity loss may be due to the diffusion and solvation of lithium polysufides into electrolyte. For the S/NHPC-1 cathode, a better electrochemical performance is achieved. It exhibits a capacity 1341 mAh/g in the initial discharge processes, and then drops to 1010 mAh/g at 20th cycle. The capacity of 847 mAh/g at 50th cycle is observed. It shows in subsequent cycles, remaining a capacity of 695 mAh/g at 100th cycle. The coulombic efficiency remains more than 99% in the whole cycling processes. The higher capacity and coulombic efficiency indicate a further suppression of shuttle effect. For the S/NHPC-1 cathode, the homogenously inlaid N atom shows a strong interaction with sulfur species to prevent its diffusion [58]. We display the cycling performance of the S/HKC, pure S and S/NHPC-1 cathodes at current density of 0.5 C in a voltage range of 1.5–3.0 V, shown in Fig. 6(c). For the S/HKC cathodes, only a low initial discharge capacity of 352 mAh/g is obtained. Then it drops to 318 mAh/ g in the 20th cycle, finally gradually decreases to 283 mAh/g after 100 cycles. Obviously, the pure sulfur exhibits the worst performance, only 197 mAh/g after 100 cycles. The capacity loss may be due to the diffusion and solvation of lithium polysufides into electrolyte. For the S/NHPC-1 cathode, a better electrochemical performance is achieved. It exhibits a capacity 1341 mAh/g in the initial discharge processes, and then drops to 1010 mAh/g at 20th cycle. The capacity of 847 mAh/g at 50th cycle is observed. It shows in subsequent cycles, remaining a capacity of 695 mAh/g at 100th cycle. The coulombic efficiency remains more than 99% in the whole cycling processes. The higher capacity and coulombic efficiency indicate a further suppression of shuttle effect. Furthermore, as shown in Fig. 6(b), the discharge and charge plateaus can be easily distinguished at different current densities (0.2–5 C), also showing good rate capability performance. Fig. 6(d) presents the rate performance of S/NHPC-1 during cycling at discharge current rates of 0.2, 0.5, 1, 2, 3, 4 and 5 C, the cathode delivers the capacities of 974, 752, 656, 538, 446, 384 and 349 mAh/g, respectively. After the high current density at 5 C and switching back to 0.2 C, it still exhibits a high capacity of 812 mAh/g, implying the stable nanostructure of S/NHPC-1. Comparatively, at the current rate of 5 C, the capacity of S/HKC is only 148 mAh/g, demonstrating the available capacities of S/NHPC-1 were averagely 200–400 mAh/g higher than that of S/HKC. The pure S showed the worst capacity compared with the carbon containing materials (S/HKC, S/NHPC-1). As the practical application of lithium-sulfur batteries, capacity retention, stability and decay rates are critical during the long-term cycling. The cycling performance of S/NHPC-1 at 1 C is shown in Fig. 6(e). After activation process, the discharge capacity of S/NHPC-1 is 593 mAh/g and a value of 354 mAh/g capacity is still kept over 500 cycles, with a slow capacity decay of ≈0.08% per cycle. Meanwhile, the coulombic efficiency of S/NHPC-1 was maintained over 95% during charge/discharge. The rate capability and decay rates of S/NHPC-1 obtained in this work were compared with some previous literature with N-doped or hierarchical structure carbon materials (Fig. S9).

For further study the stability and electrochemical characteristics of the MOF aerogel derived carbon materials, S/HKC and S/NHPC-1 cathodes were verified by electrochemical impedance spectroscopy (EIS) (Fig. 7). The equivalent electrical circuit of data is shown in Table 1. It is observed that, the S/NHPC-1 cathode exhibited a lower charge transfer resistance (47.53 Ω) than that of the S/HKC (67.88 Ω) before cycle, corresponding to smaller semicircles

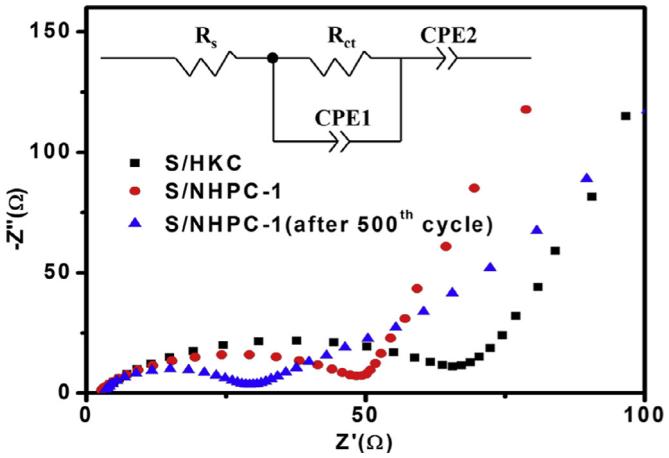

Fig. 7. EIS curves of the S/NHPC-1 cathode before and after 500 cycles at 1 C and S/HKC (inset: the equivalent electrical circuit).

Table 1. The equivalent electrical circuit of experimental data.

Impedance values	R_s (Ω cm^{-2})	R_{ct} (Ω cm^{-2})
S/HKC	3.682	67.88
S/NHPC-1	3.238	47.53
S/NHPC-1 (after 500th cycles)	4.416	41.21

under high and middle frequency. This indicates that the S/NHPC-1 possesses fast reaction kinetics during the charge/discharge, which could be attributed to the rod-like nanostructure and N-doped. Over 500 cycles, as shown in Fig. 7, the resistance of the S/NHPC-1 slightly decreases, which may result from the redistribution of LiPS and chemical activation process, implying a closer contact and better coverage between the active material and the hosts [21].

The performances of the carbon materials derived from MOF aerogel under different conditions in the lithium sulfur batteries are investigated. As shown in Fig. 8(a), the initial capacities of these composites, including S/NHPC-0.1, S/NHPC-0.5, S/NHPC-1 and S/NHPC-2, are greatly different, which is attributed to their different nitrogen contents and structures [7,55]. Among these samples investigated, the S/NHPC-1 possesses the mediate nitrogen content (6.4 wt%), however, it exhibits the highest initial capacity of 1341 mAh/g (Table S1). And over 100 cycles, the S/NHPC-1 exhibits the best cyclic stability at 0.5 C. As mentioned above, there are abundant mesopores in the NHPC-1 in addition to its mediate nitrogen doping. The hierarchical porous structures and nitrogen doping active sites have strong immobilizing ability for the sulfur species, thus limiting effectively polysulfide dissolution [51,59]. The rate capabilities of these composites are shown in Fig. 8(b). After 10 cycles at 0.2 C, the S/NHPC-1 exhibits the highest reversible capacity of 973 mAh/g. At the rate of 5 C, it still delivers a high capacity of 353 mAh/g, much higher than those of other samples. In addition, Fig. 8(c)–(d) shows the cycle and rate performance of lithium-sulfur batteries with NHPC cathodes prepared at different temperatures. The NHPC-1 cathodes are fabricated from MOA-1 calcined at 600, 700, 800 and 900 °C, denoted as 600-NHPC-1, 700-NHPC-1, 800-NHPC-1 and 900-NHPC-1, respectively. The batteries with the 600-S/NHPC-1, 700-S/NHPC-1, 800-S/NHPC-1 and 900-S/NHPC-1 cathodes deliver the discharge specific capacities of 422, 523, 476 and 315 mAh/g at 0.5 C, respectively, over 100 cycles. The rate capabilities of the 600-S/NHPC-1, 700-S/NHPC-1, 800-S/NHPC-1 and 900-S/NHPC-1 cathodes are depicted in Fig. 8. At the maximum rate of 5 C, the specific capacities of batteries with these cathodes are 132, 320, 200 and 112 mAh/g, respectively. The 700-S/NHPC-1 evidently displays superior cycle stability and

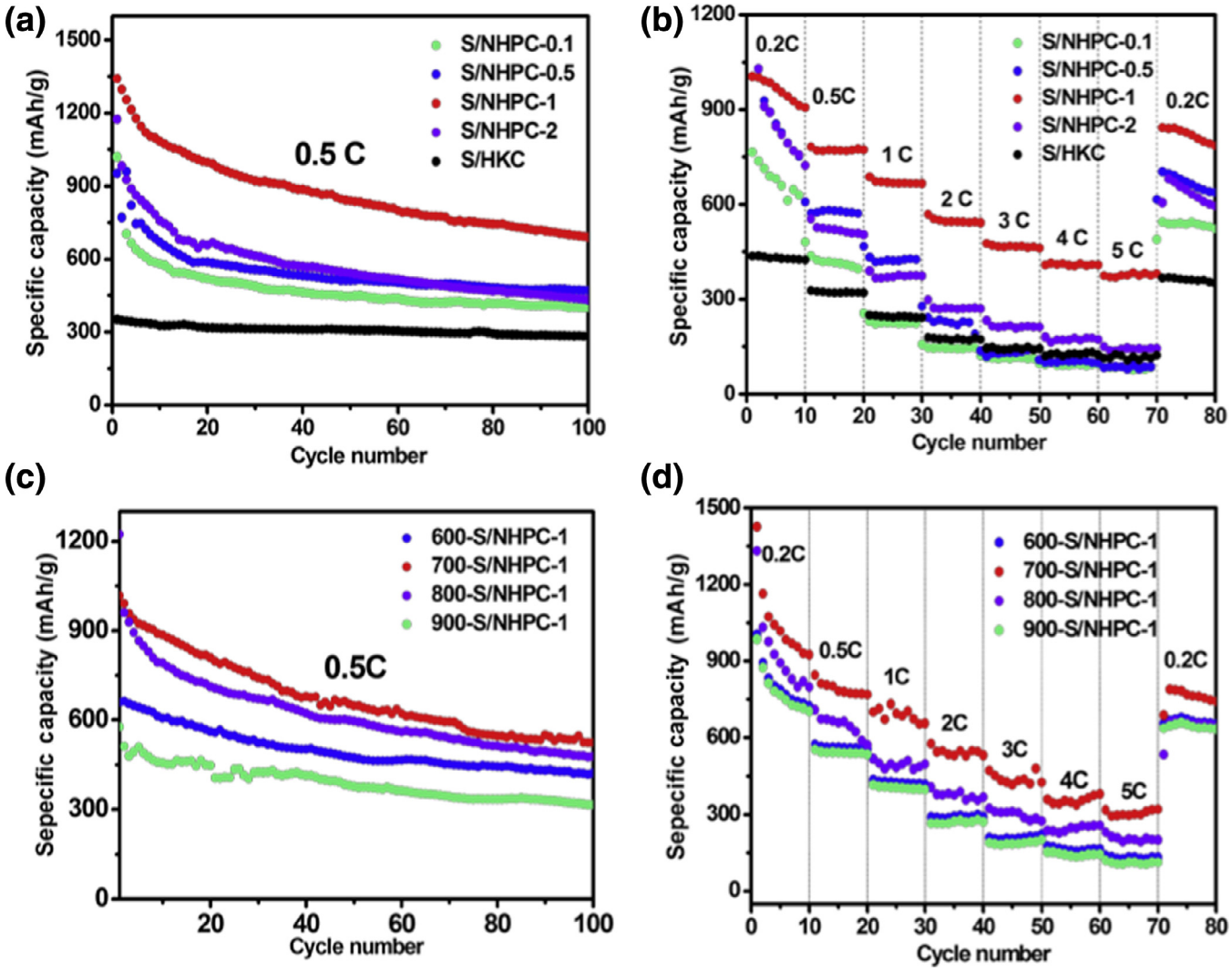

Fig. 8. (a, b) The cycle stability of batteries and rate performance of S/NHPC-*x* composites with different HMT contents. (c, d) The cycle stability of batteries with the S/NHPC-1 and charging/discharging curves at 0.2, 0.5, 1, 2, 3, 4 and 5 C of the materials obtained at different carbonization temperatures.

rate capability compared with the carbon materials from other carbonization temperatures.

4. Conclusions

In summary, a series of novel well-designed N-doped hierarchical porous carbons have been created from metal organic gels and show outstanding electrochemical performance. The electrode could retain a discharge capacity of 349 mAh/g at a discharge rate of 5 C. The electrode manifests stable long-term cyclic performance and remains at 354 mAh/g up to 500 cycles at 1 C, with an ultralow decay ratio≈0.08% per cycle and a high average coulombic efficiency over 95%. The excellent rate capability and remarkable long-term cyclability of the S/NHPC-1 cathode are attributed to its hierarchical porous structures for confining the soluble LiPS and 1D rod-like integrated carbon networks for supplying electrons with “green channels”, as well as the nitrogen doping for high absorbability of LiPS.

Acknowledgments

This work is supported by the National Natural Science Foundation of China (Grant no. U1610105, 51672033, U1610255), the Natural Science Foundation of Liaoning Province (201602170), the Open Fund of Key Laboratory of Interface Science and Engineering in Advanced Materials, Ministry of Education (KLISEAM 201601), and the Open Sharing Fund Projects for Large Equipments Testing, Dalian University of Technology (2016-54).

Supplementary materials

Supplementary material associated with this article can be found, in the online version, at doi:10.1016/j.jechem.2017.08.016.

References

[1] P.G. Bruce, S.A. Freunberger, L.J. Hardwick, J.M, Nat. Mater. 11 (2012) 19–29.
[2] M. Zhang, C. Yu, C. Zhao, X. Song, X. Han, S. Liu, C. Hao, J. Qiu, Energy Storage Mater. 5 (2016) 223–229.
[3] X. Ji, K.T. Lee, L.F. Nazar, Nat. Mater. 8 (2009) 500–506.
[4] M. Wild, L. O'Neill, T. Zhang, R. Purkayastha, G. Minton, M. Marinescu, G.J. Offer, Energy Environ. Sci. 8 (2015) 3477–3494.
[5] G. Li, J. Sun, W. Hou, S. Jiang, Y. Huang, J. Geng, Nat. Commun. 7 (2016) 10601.
[6] Z. Zheng, H. Guo, F. Pei, X. Zhang, X. Chen, X. Fang, T. Wang, N. Zheng, Adv. Funct. Mater. 11 (2016) 8952–8959.
[7] X. Wang, Z. Zhang, Y. Qu, Y. Lai, J. Li, J. Power Sources 256 (2014) 361–368.
[8] T.-Z. Hou, H.-J. Peng, J.-Q. Huang, Q. Zhang, B. Li, 2D Mater. 2 (2015) 014011.
[9] Y. Qiu, W. Li, W. Zhao, G. Li, Y. Hou, M. Liu, L. Zhou, F. Ye, H. Li, Z. Wei, S. Yang, W. Duan, Y. Ye, J. Guo, Y. Zhang, Nano Lett. 14 (2014) 4821–4827.
[10] G. Zhou, L. Li, C. Ma, S. Wang, Y. Shi, N. Koratkar, W. Ren, F. Li, H.-M. Cheng, Nano Energy 11 (2015) 356–365.

[11] J. Yang, J. Xie, X. Zhou, Y. Zou, J. Tang, S. Wang, F. Chen, L. Wang, J. Phys. Chem. C 118 (2014) 1800–1807.
[12] L. Ji, M. Rao, S. Aloni, L. Wang, E.J. Cairns, Y. Zhang, Energy Environ. Sci. 4 (2011) 5053.
[13] J.S. Lee, W. Kim, J. Jang, A. Manthiram, Adv. Energy Mater. 13 (2016) 1601943.
[14] S.H. Chung, C.H. Chang, A. Manthiram, ACS Nano 10 (2016) 10462–10470.
[15] F. Jin, S. Xiao, L. Lu, Y. Wang, Nano Lett. 16 (2016) 440–447.
[16] L. Sun, D. Wang, Y. Luo, K. Wang, W. Kong, Y. Wu, L. Zhang, K. Jiang, Q. Li, Y. Zhang, J. Wang, S. Fan, ACS Nano 10 (2016) 1300–1308.
[17] Q. Fan, W. Liu, Z. Weng, Y. Sun, H. Wang, J. Am. Chem. Soc. 137 (2015) 12946–12953.
[18] H.-J. Peng, T.-Z. Hou, Q. Zhang, J.-Q. Huang, X.-B. Cheng, M.-Q. Guo, Z. Yuan, L.-Y. He, F. Wei, Adv. Mater. Interfaces 1 (2014) 1400227.
[19] M. Wang, W. Wang, A. Wang, K. Yuan, L. Miao, X. Zhang, Y. Huang, Z. Yu, J. Qiu, Chem. Commun. 49 (2013) 10263–10265.
[20] S. Niu, W. Lv, C. Zhang, Y. Shi, J. Zhao, B. Li, Q.-H. Yang, F. Kang, J. Power Sources 295 (2015) 182–189.
[21] Z. Li, C. Li, X. Ge, J. Ma, Z. Zhang, Q. Li, C. Wang, L. Yin, Nano Energy 23 (2016) 15–26.
[22] Z. Wang, Y. Dong, H. Li, Z. Zhao, H.B. Wu, C. Hao, S. Liu, J. Qiu, X.W. Lou, Nat. Commun. 5 (2014) 5002.
[23] X. Zhang, X. Cheng, Q. Zhang, J. Energy Chem. 25 (2016) 967–984.
[24] Z. Wei Seh, W. Li, J.J. Cha, G. Zheng, Y. Yang, M.T. McDowell, P.C. Hsu, Y. Cui, Nat. Commun. 4 (2013) 1331.
[25] X. Liang, L.F. Nazar, ACS Nano 10 (2016) 4192–4198.
[26] Z. Li, J. Zhang, X.W. Lou, Angewandte Chemie. 54 (2015) 12886–12890.
[27] X. Tao, J. Wang, Z. Ying, Q. Cai, G. Zheng, Y. Gan, H. Huang, Y. Xia, C. Liang, W. Zhang, Y. Cui, Nano Lett. 14 (2014) 5288–5294.
[28] H. Wei, E.F. Rodriguez, A.S. Best, A.F. Hollenkamp, D. Chen, R.A. Caruso, Adv. Energy Mater. 7 (2016) 1601616.
[29] S. Rehman, S. Guo, Y. Hou, Adv. Mater. 28 (2016) 3167–3172.
[30] H. Yao, G. Zheng, P.C. Hsu, D. Kong, J.J. Cha, W. Li, Z.W. Seh, M.T. McDowell, K. Yan, Z. Liang, V.K. Narasimhan, Y. Cui, Nat. Commun. 5 (2014) 3943.
[31] Z.W. Seh, J.H. Yu, W. Li, P.C. Hsu, H. Wang, Y. Sun, H. Yao, Q. Zhang, Y. Cui, Nat. Commun. 5 (2014) 5017.
[32] T. Lei, W. Chen, J. Huang, C. Yan, H. Sun, C. Wang, W. Zhang, Y. Li, J. Xiong, Adv. Energy Mater. 7 (2016) 1601843.
[33] X. Liang, A. Garsuch, L.F. Nazar, Angewandte Chemie. 54 (2015) 3907–3911.
[34] J. Zhang, H. Hu, Z. Li, X.W. Lou, Angewandte Chemie. 55 (2016) 3982–3986.
[35] X. Yang, Y. Yu, N. Yan, H. Zhang, X. Li, H. Zhang, J. Mater. Chem. A 4 (2016) 5965–5972.
[36] J. Zheng, J. Tian, D. Wu, M. Gu, W. Xu, C. Wang, F. Gao, M.H. Engelhard, J.G. Zhang, J. Liu, J. Xiao, Nano Lett. 14 (2014) 2345–2352.
[37] J. Zhou, R. Li, X. Fan, Y. Chen, R. Han, W. Li, J. Zheng, B. Wang, X. Li, Energy Environ. Sci. 7 (2014) 2715.
[38] T.Z. Hou, X. Chen, H.J. Peng, J.Q. Huang, B.Q. Li, Q. Zhang, B. Li, Small 12 (2016) 3283–3291.
[39] L. Li, G. Zhou, L. Yin, N. Koratkar, F. Li, H.-M. Cheng, Carbon 108 (2016) 120–126.
[40] J. Song, M.L. Gordin, T. Xu, S. Chen, Z. Yu, H. Sohn, J. Lu, Y. Ren, Y. Duan, D. Wang, Angewandte Chemie. 54 (2015) 4325–4329.
[41] W. Xia, B. Qiu, D. Xia, R. Zou, Sci. Rep. 3 (2013) 1935.
[42] J. Tang, Y. Yamauchi, Nat. Chem. 8 (2016) 638–639.
[43] G. Xu, B. Ding, L. Shen, P. Nie, J. Han, X. Zhang, J. Mater. Chem. A 1 (2013) 4490.
[44] Y. Liu, G. Li, Z. Chen, X. Peng, J. Mater. Chem. A 5 (2017) 9775–9784.
[45] S. You, X. Gong, W. Wang, D. Qi, X. Wang, X. Chen, N. Ren, Adv. Energy Mater. 6 (2016) 1501497.
[46] Y.Z. Chen, C. Wang, Z.Y. Wu, Y. Xiong, Q. Xu, S.H. Yu, H.L. Jiang, Adv. Mater. 27 (2015) 5010–5016.
[47] H.B. Wu, B.Y. Xia, L. Yu, X.Y. Yu, X.W. Lou, Nat. Commun. 6 (2015) 6512.
[48] L. Li, S. Xiang, S. Cao, J. Zhang, G. Ouyang, L. Chen, C.Y. Su, Nat. Commun. 4 (2013) 1774.
[49] D. Jiang, A. Urakawa, M. Yulikov, T. Mallat, G. Jeschke, A. Baiker, Chemistry 15 (2009) 12255–12262.
[50] Q.-X. Luo, B.-W. An, M. Ji, S.-E. Park, C. Hao, Y.-Q. Li, J. Porous Mater. 22 (2014) 247–259.
[51] R. Chen, T. Zhao, J. Lu, F. Wu, L. Li, J. Chen, G. Tan, Y. Ye, K. Amine, Nano Lett. 13 (2013) 4642–4649.
[52] Z. Yuan, H.-J. Peng, J.-Q. Huang, X.-Y. Liu, D.-W. Wang, X.-B. Cheng, Q. Zhang, Adv. Funct. Mater. 24 (2014) 6105–6112.
[53] Q. Pang, J. Tang, H. Huang, X. Liang, C. Hart, K.C. Tam, L.F. Nazar, Adv. Mater. 27 (2015) 6021–6028.
[54] Z. Li, L. Yin, ACS Appl. Mater. Interfaces 7 (2015) 4029–4038.
[55] F. Sun, J. Wang, H. Chen, W. Li, W. Qiao, D. Long, L. Ling, ACS Appl. Mater. Interfaces 5 (2013) 5630–5638.
[56] H. Xu, Y. Deng, Z. Zhao, H. Xu, X. Qin, G. Chen, Chem. Commun. 50 (2014) 10468–10470.
[57] Y. Liu, X. Wang, Y. Dong, Y. Tang, L. Wang, D. Jia, Z. Zhao, J. Qiu, Chem. Commun. 52 (2016) 12825–12828.
[58] Z. Li, L. Yuan, Z. Yi, Y. Liu, Y. Xin, Z. Zhang, Y. Huang, Nanoscale 6 (2014) 1653–1660.
[59] J.J. Chen, Q. Zhang, Y.N. Shi, L.L. Qin, Y. Cao, M.S. Zheng, Q.F. Dong, Phys. Chem. Chem. Phys. 14 (2012) 5376–5382.